



Cite this: *Nanoscale*, 2021, **13**, 11994

Structural reconstruction and visible-light absorption *versus* internal electrostatic field in two-dimensional GaN–ZnO alloys†

Hanpu Liang and Yifeng Duan *

GaN–ZnO alloys are more promising semiconductors than their counterparts for optoelectronic applications due to the abrupt red shift in the visible-light range. Unfortunately, the strong internal electrostatic field (IEF) seriously hinders to further improve the optoelectronic performance due to the charge density of surface states. We point out a structural model to extremely improve the visible-light absorption by overcoming the bottleneck of the IEF in the two-dimensional (2D) nonisovalent alloys. The novel haeckelite (8|4) configuration with the nearly zero IEF shows much better optoelectronic performances than the conventional wurtzite configuration. Meanwhile, we explore the thickness-driven structural transitions from the planar hexagonal to the 8|4 and to the wurtzite configurations. The visible-light absorption efficiency quickly rises up from the bulk wurtzite to the bulk 8|4 to the 2D 8|4 and to the MoS₂-based heterostructures with the different-layer 8|4 configurations. The heterointerfacial coupling is an effective way to further reduce the IEF and hence to significantly improve the visible-light absorptions by enlarging the population of band edge states in the 8|4 configuration. We suggest that the 8|4 configuration is more prospective for diverse optoelectronic applications in 2D GaN–ZnO alloys than in binary counterparts.

Received 22nd April 2021,
Accepted 28th June 2021

DOI: 10.1039/d1nr02548a

rsc.li/nanoscale

1. Introduction

GaN-based semiconductors are highlighted for the outstanding properties that lead to a variety of applications in electronics and optoelectronics.¹ The optoelectronic efficiency is seriously harmed by the IEF produced by the opposite polarization charges on the [0001] and [000–1] surfaces. It stems from the anomalous *c:a* ratio, the lack of inversion symmetry, and the ionic characters of covalent bonds in the wurtzite structure.^{2,3} The IEF markedly changes the band-edge shapes near the valence-band maximum (VBM) and the conduction-band minimum (CBM), according to the Stark effects.⁴ Nonpolar phases, *e.g.*, the zinc blende structure, were attempted to be utilized in lighting devices,⁵ however, such structures are always thermodynamically metastable. To reduce the IEF effects, it is urgent to seek out a novel configuration, where the adjacent dipoles counteract spontaneously.

2D semiconductors possess the potential to ultimately minimize the size of devices and to drastically reduce the energy consumption. The progress of layered materials^{6,7} has greatly inspired interests in the mono- and few-layer structures

of conventional III–V semiconductors as a new class of 2D materials, which is intrinsically distinct from the easily cleaved van der Waals (vdW) materials. 2D vdW GaN has been extensively studied by differently stacking the planar graphitic configurations,^{8–11} as in 2D TMDC, graphite or h-BN.^{12,13} Recent investigations propose that, in 2D III–V semiconductors, the graphitic and wurtzite structures spontaneously reconstruct into the haeckelite (8|4) configuration in the few layer limit.¹⁴ It is hexagonal in plane and the alternating octagons and squares are formed by interlayer covalent bonds. In ideal 8|4 structure, the charged surfaces becomes neutral, and hence the IEF is zero. Therefore, the 8|4 configuration is expected to possess better optoelectronic performances than the wurtzite configurations.

Experimental syntheses have obtained great successes in the epitaxial growths of 2D semiconductors, for example, AlN on Ag(111),^{15,16} GaN on graphene,^{17,18} and ZnO on Ag(111) substrate.¹⁹ However, the samples share either the graphitelike or the wurtzite configuration and the synthesis of the 8|4 configuration is still a challenge. Although the 8|4 structure is mainly studied at the theoretical level at present,^{14,20–22} the huge progresses in 2D-material synthesis have inspired growing interests. In addition, the present studies focus on 2D III–V or II–VI semiconductors, not on their 2D pseudobinary nonisovalent III–V/II–VI alloys.

Alloying usually introduces novel performances in the light absorption/emission, compared to the counterparts. For

School of Materials and Physics, China University of Mining and Technology, Xuzhou, Jiangsu 221116, China. E-mail: yifeng@cumt.edu.cn

† Electronic supplementary information (ESI) available. See DOI: 10.1039/D1NR02548A

instance, the direct band gap is 2.40 eV in $(\text{GaN})_{0.5}(\text{ZnO})_{0.5}$,^{23,24} while are 3.40 and 3.20 eV in GaN and ZnO, respectively, thus more suitable in lighting devices. In addition, atomic-scale semiconductors always behave different properties from the bulk counterparts thus paving the way to conceptually novel devices. Therefore, it is technologically necessary to deeply explore 2D GaN–ZnO alloys to widen the optoelectronic applications. Because of the complexity in atomic species and electronegativity, it is hard to completely eliminate the IEF in the 8|4 configuration. The detailed properties, together with underlying mechanisms, await to be further investigated.

In this work, first, we search the stable configurations of 2D GaN–ZnO alloys in the mono- and few-layer limits using an evolutionary variable-composition search based on first-principles calculations. Except for the bulk 1:1 stoichiometry, no other bulk or 2D phases/structures have been reported. In theory, GaN and ZnO could combine in various ways, since they share the same wurtzite symmetry, very close lattice constants, and near electronegativity for cations and anions. Second, we reveal how the IEF change with the configuration and the number of layers in order to point out a feasible way to eliminate the IEF effects and hence to greatly enhance the visible-light absorption. Finally, we display the effects of the heterointerfacial coupling and the number of the 8|4 layers on the structural stability and the visible-light absorption in the MoS₂-based heterostructures to widen the optoelectronic applications.

2. Computational methods

Structural searches for stable phases were carried out *via* the USPEX code,^{25,26} in combination with structural relaxations and total energy calculations within the PBE approximation²⁷ based on the density functional theory (DFT),²⁸ as implemented in the VASP package.^{29,30} The vdW interaction was considered by the vdW-DF2 exchange functional.³¹ Force constants for phonon calculations and *ab initio* molecular dynamics for the temperature effect on the structural transition were carried out using the VASP. On the basis of the calculated force constants, phonon dispersions were obtained with the PHONOPY code.³² The electronic band structures and optical absorption spectra were obtained by the PWmat code^{33,34} within the HSE06 hybrid functional.³⁵ The plane-wave energy cutoff of 500 eV and the Γ -centered k -meshes of $2\pi \times 0.05 \text{ \AA}^{-1}$ resolution for Brillouin zone sampling were adopted to ensure excellent convergence of total energies. The G_0W_0 -BSE³⁶ procedure is used to calculate the exciton effects in optical absorption spectra. Test calculations show that a k grid of $8 \times 8 \times 4$ and 288 conduction bands in the G_0W_0 calculations converge the band gap within 1 meV.

During the structural searches, the first and the remaining generations had 300 and 100 structures, respectively, which were produced randomly with up to 30 atoms for the variable-composition search and 33 atoms per unit cell for the fixed-

composition search. The succeeding generation were obtained by applying heredity (35%), soft mutation (15%), and transmutation (15%) operators, respectively, the rest of each generation was produced randomly from space groups.

According to the band theory, the optical absorption originates from the electron–hole pair,^{37–39} which is coupled by the Coulomb potential expressed as

$$V(\vec{r}) = -\frac{e^2}{\epsilon r} - e\vec{\mathcal{E}} \cdot \vec{r}, \quad (1)$$

where \vec{r} is the distance between the electron and hole, ϵ is the dielectric constant, and $\vec{\mathcal{E}}$ is the electric field. First, the bound levels are mixed and broadened due to the lower lip of the potential well by the effect of the electric field, as illustrated in Fig. 1. Second, the electric field produces the second-order Stark effect due to the slightly widened Coulomb well. Based on the effective-mass approximation and the isotropy near the band edge, the equation is simplified as

$$\left(-\frac{\hbar^2}{2\mu} \nabla^2 - V(\vec{r}) \right) \phi_n(\vec{r}) = \left(E_n - \frac{\hbar^2 K^2}{2M} \right) \phi_n(\vec{r}), \quad (2)$$

where $E_n = E - E_g$, E_g is the energy gap, μ and M are the reduced mass and the sum of the electron and hole masses, respectively, and $\phi_n(r)$ is

$$\phi_n(\vec{r}) = \Phi_{c,v}^{n,\vec{K}}(\vec{r}_e, \vec{r}_h) e^{-i\vec{K} \cdot \vec{R}}. \quad (3)$$

Eqn (2) determines the wave function of the Wannier exciton in an electric field, which is approximately treated as a linear combination of Bloch functions of the electron and hole as follows

$$\Phi_{c,v}^{n,\vec{K}}(\vec{r}_e, \vec{r}_h) = \sum_{\vec{k}_e} \sum_{\vec{k}_h} e^{i\vec{k}_e \cdot \vec{k}_e} e^{i\vec{k}_h \cdot \vec{k}_h} A_{c,v}^{n,\vec{K}}(\vec{k}_e, \vec{k}_h). \quad (4)$$

The optical transition rate from the ground state Ψ_0 to the excited state $\Psi^{n,\vec{K}}$ in the entire spectra is determined by the matrix element⁴⁰

$$M^{n,\vec{K}} = \langle \Psi^{n,\vec{K}} | (ie\hbar\vec{A}/mc) e^{i\vec{q} \cdot \vec{r}} \cdot \nabla | \Psi_0 \rangle, \quad (5)$$

where $\vec{A} = A\hat{e}e^{i\vec{q} \cdot \vec{r} - i\omega t}$ is the vector potential of the electromagnetic wave. Neglecting the momentum of the photon $\hbar\vec{q}$ rela-

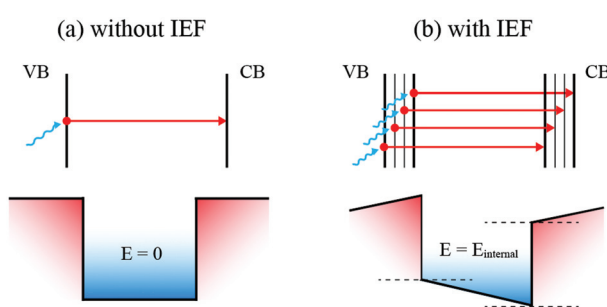


Fig. 1 Electronic transition and the Coulomb potential (a) without IEF and (b) with IEF.

tive to the crystal momentum $\hbar\vec{k}$, the matrix element is further simplified as

$$M^{n,\vec{K}} = \sum_{c,v} \left(\frac{ie\hbar A}{mc} \right) \delta_{\vec{K},0} \times \left(\frac{i\hat{e}}{\hbar} \cdot \vec{P}_{cv} \phi_n(0) + U_{cv} |\hat{e} \cdot \nabla \phi_n|_{r=0} \right), \quad (6)$$

where $\vec{P}_{cv} = (\hbar/i) \int_{\Omega} d\vec{r} u_{c,\vec{k}}^* \nabla u_{v,\vec{k}}$ and $U_{cv} = \int_{\Omega} d\vec{r} u_{c,\vec{k}}^* u_{v,\vec{k}}$.

The imaginary part of the dielectric constant is achieved by the $M^{n,\vec{K}}$

$$\epsilon_2 = \frac{4\pi^2 c^2}{\omega^2 A^2} \sum_{\vec{K}, n, c, v} |M^{n,\vec{K}}|^2 \delta(E - \hbar\omega). \quad (7)$$

For allowed transitions, u_c and u_v are antisymmetric and $U_{cv} \approx 0$, thus ϵ_2 is given by⁴¹

$$\epsilon_2 = \frac{4\pi^2 e^2}{m^2 \omega^2} \sum_{c,v,\vec{K},0} \delta_{\vec{K},0} |\hat{e} \cdot \vec{P}_{cv}|^2 |\phi_n(0)|^2 \delta(E_g + E_n - \hbar\omega). \quad (8)$$

The absorption coefficient α , proportional to the wave function square of the final state at the origin $|\phi_n(0)|^2$, is decided by the imaginary part of the dielectric constant, i.e., $\alpha = \epsilon_2 \omega / nc$, where n is the index of reflection.

3. Results and discussion

We first identify the stable bulk phases of GaN–ZnO alloys and plot the complete convex hull at ambient pressure in Fig. 2(a). By definition, a structure on the convex hull is thermodynamically stable, while a structure with negative formation enthalpy but above the hull is metastable. The ground-state phase exists at the 1 : 1 stoichiometry and shares the wurtzite $P3m1$ symmetry. More interestingly, at this stoichiometry, a metastable haecelelite (8|4) $Pmn2_1$ phase is just above the $P3m1$ by 3.16 meV per atom. The comparable absorption thresholds originate from the direct band gaps of 2.43 and 2.34 eV in the 8|4 and wurtzite configurations, respectively (see Fig. 2 and S1 in the ESI†⁴²). In theory, the optical absorption strongly depends on the transition probability amplitude,⁴³ i.e., $\alpha(\omega) = \text{const} \times |\phi_n(0)|^2$, where $\phi_n(0)$ is proportional to the inverse of electric field. Owing to the nearly zero IEF, the band edge absorption intensity is stronger at least 55% in the 8|4 configuration than in the polar wurtzite configuration. The main absorption peaks all appear around 3.20 eV (near the band gaps of binary counterparts), and the intensity is 75% stronger in the 8|4 configuration. Therefore, the 8|4 configuration is more suitable for applications in lighting devices than the wurtzite configuration. Moreover, the electron–hole interaction is considered in the optical absorption (see Fig. 2(b) and (c)). The exciton binding energies of bulk 8|4 and wurtzite phases are 182 and 225 meV with the k grids of $12 \times 12 \times 6$ and $12 \times 12 \times 8$, respectively, which converge within 20 meV (see Fig. S2 in ESI†).

The structural details are displayed as inserts in Fig. 2(a) and listed in Table S1 in ESI.† In the wurtzite structure, due to the difference in atomic species and electronegativity, the

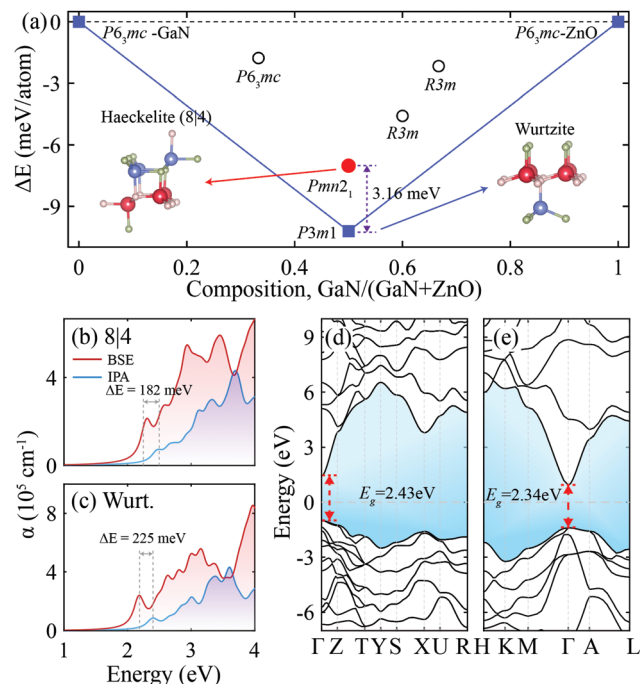


Fig. 2 (a) Convex hull of bulk GaN–ZnO system at ambient pressure. Optical absorption coefficients with (red line) and without (blue line) electron–hole interactions for bulk (b) haecelelite 8|4 and (c) wurtzite phases, together with the electronic band structures for the (d) 8|4 and (e) wurtzite structures, with the structural details as insets in panel (a). The k grids of $12 \times 12 \times 6$ and $12 \times 12 \times 8$ are adopted in the G_0W_0 –BSE calculations for the bulk 8|4 and wurtzite structures, respectively.

bond angles in the tetrahedron are $\sim 106^\circ$ and $\sim 112^\circ$, derived from $\sim 109^\circ$ of binary semiconductors. In the 8|4 structure, one angle continuously decreases to $\sim 93^\circ$ to form the square and octagonal motifs, and the others increase to $\sim 109^\circ$ and $\sim 114^\circ$ to maintain the honeycomb configurations. The structural distortions tend to destabilize the 8|4 structure. Meanwhile, the adjacent dipoles have opposite directions along the c axis, thereby, the nearly zero total dipole moments stabilize the 8|4 structure.

Phonon spectra of the bulk 8|4 and wurtzite phases are displayed in Fig. S3 in ESI.† the absence of any imaginary phonon modes indicates the dynamical stability. Therefore, it is promising to experimentally synthesize these phases, which are adopted herein for further investigations. In addition, other metastable phases probably occur at 1 : 2, 2 : 1 and 3 : 2 stoichiometries. The excellent optoelectronic performances in the bulk 8|4 phase inspire us to deeply dig out the visible-light absorption in 2D alloys at the 1 : 1 stoichiometry.

Fig. 3(a) displays the relative energy for predicted phases to reveal the thermodynamical stability at different thicknesses. The ground state is the planar hexagonal structure in monolayer, and the 8|4 structure when the thickness is between 2 and 24 layers. Once the number of layers exceeds 24, the wurtzite structure is the most stable. The structural stability is evaluated by the phonon spectra at ambient conditions for the

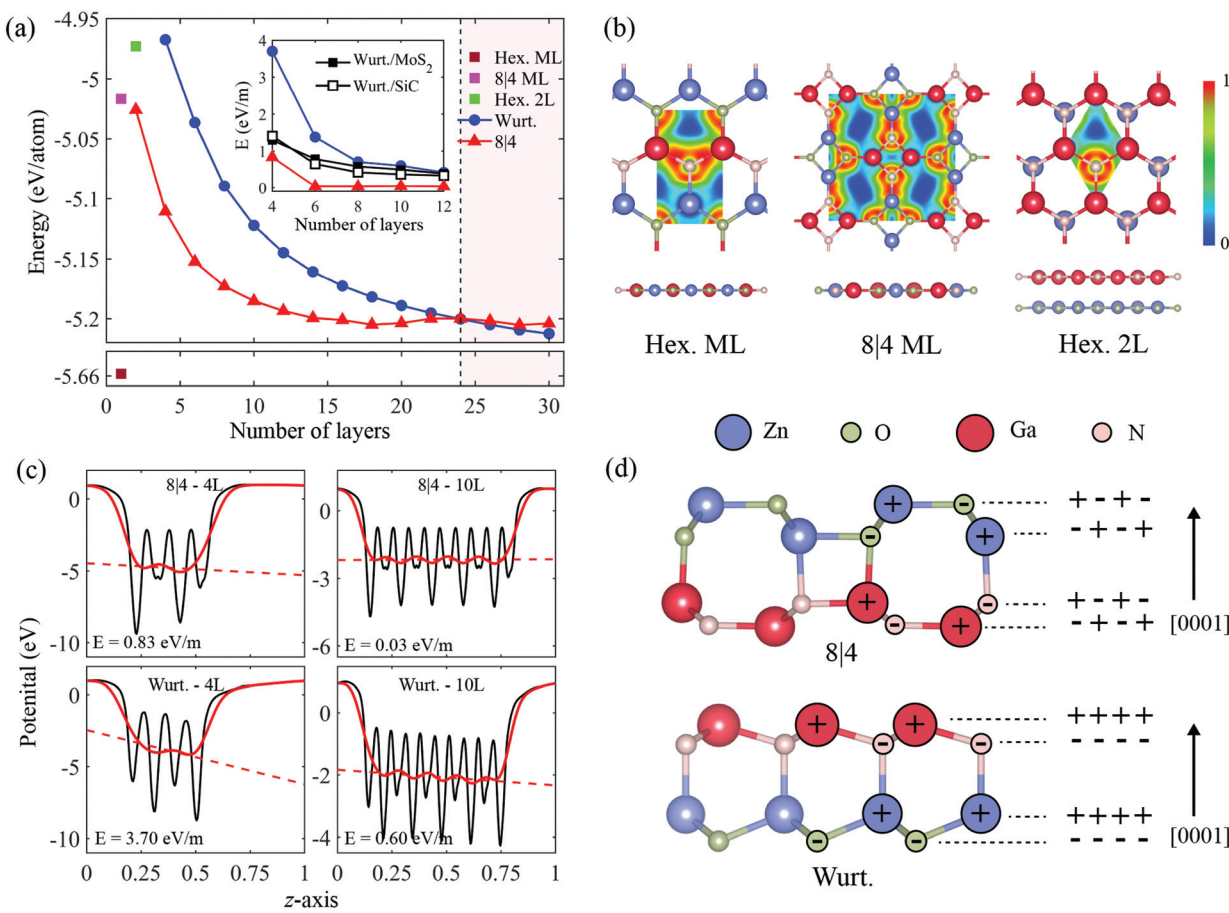


Fig. 3 (a) Total energy per atom as a function of the number of layers in the wurtzite and haackelite 8|4 configurations. (b) Monolayer hexagonal and 8|4, and two-layer hexagonal configurations, together with the electron localization functions. (c) Planar- (black line) and macroscopic-average (red line) internal electrostatic potentials along the c axis at different GaN–ZnO thicknesses in the 8|4 and wurtzite configurations. (d) Two-dimensional views along the a axis and the schemes of charge distribution along the c axis in the multilayer 8|4 and wurtzite configurations.

hexagonal and 8|4 phases up to ten layers (see Fig. S4 in ESI†). No any imaginary frequencies in the whole Brillouin zone (BZ) suggest the dynamical stability. We further construct the two-, four- and six-layer wurtzite configurations with different stacking modes, as illustrated in Fig. S5 in ESI,† and confirm that the 8|4 configuration is more stable in energy, *e.g.*, by at least 53 meV per atom than two-layer AA-stacking hexagonal configuration, the details of the relative energy are listed in Table S2 in ESI.†

Fixed-composition searches confirm the monolayer planar hexagonal configuration is more energetically favorable than the monolayer 8|4 configuration with the energy of -679 and -37.1 meV per atom, respectively. In the hexagonal structure, the triangle-planar coordination is formed by the sp² hybridization with the bond angles of 118.37° and 123.26° (see Fig. 3(b)). The nearly zero total dipole moments in the monolayer hexagonal configuration markedly reduce the system energy. In the 8|4 structure, the strong structural distortions to form the squares make the energy to rise up, although the dipole moments are also neutralized by the opposite directions of adjacent dipoles.

During the structural relaxation, the two-layer wurtzite structure is treated as the initial configuration, the planar hexagonal vdW configuration is spontaneously constructed by the AA stacking (see Fig. 3(b)). Our structural searches reveal that the two-layer 8|4 configuration is more stable than the hexagonal vdW (vdW-DF2 exchange functional) configuration by 53 meV per atom, due to the joint effects of the nearly zero IEF and the interlayer covalent bonds. The IEF is more dominant in the structural stability than the interlayer bonds in the few-layer limit. In the initial wurtzite configuration, although the interlayer bonds exist, the strong dipoles associated with the opposite charges on surfaces destabilize the structure. On the other hand, the structural distortion in the 8|4 configuration accumulates with the number of layers, thereby, once the thickness exceeds a critical value, the wurtzite structure is more stable, due to the natural tetrahedral coordination.

Fig. 3(b) shows the spatial valence band edge state distributions of the hexagonal and monolayer 8|4 configurations, which are drastically different. In the monolayer hexagonal configuration, the valence electrons mainly exist between N and Ga atoms, reflecting the covalent nature. In the monolayer

8|4 configuration, the valence electrons are jointly dominated by N and Zn, not by N and Ga atoms. This is because that two N atoms are as close as 2.72 Å in a square, much smaller than in the hexagonal configuration, thereby the strong Coulomb repulsion pushes the valence electrons of adjacent N atoms far away each other. In the two-layer hexagonal configuration, due to the unique AA stacking mode, the valence electrons are symmetrically distributed around the N atoms. Note that the O atoms share the similar valence-electron distributions.

To deeply explore the IEF, the electrostatic potentials are calculated for the wurtzite and 8|4 phases, since the slope of its macroscopic-averaged values quantifies the IEF.²⁰ The configurations up to twelve layers are adopted to ensure the reliability (see Fig. 3(c) and S6 in ESI†). The IEFs are 3.70 and 0.83 eV m⁻¹ in the four-layer wurtzite and 8|4 configurations, respectively. In the wurtzite structure, the dipoles share the nearly same direction, leading to the huge IEF. As the number of layers increases, the IEF drops quickly to zero above six layers in the 8|4 configuration, while approaches to a converged value around 0.38 eV m⁻¹ at twelve layers in the wurtzite configuration (see insert of Fig. 3(a)).

In the few-layer 8|4 and wurtzite configurations, one layer is composed of Ga and N atoms, and the adjacent layers of Zn and O atoms, plotted in Fig. 3(d). The electrostatic potential is much lower in the Ga-N layer than in the Zn-O layer due to

the difference in valency. Since each layer is almost neutrally charged in the 8|4 configuration, the potentials are equal for the Ga-N layers, so are for the Zn-O layers, hence, the macroscopic-averaged values remain almost unchanged with the number of layers. In contrast, the positive and negative charged layers are alternately stacked in the wurtzite configuration, thereby, the potential difference exists between the adjacent Ga-N layers, so does between the adjacent Zn-O layers. The differences accumulate with increasing layer number and hence induce the strong IEF, which eventually destabilizes the few-layer wurtzite configuration.

Investigations of bulk configurations reveal that the 8|4 configuration shares the more excellent light absorptions than the wurtzite configuration, with the comparable absorption thresholds (see Fig. 2(b)). Herein, the light absorptions are calculated at the HSE06 level and plotted in Fig. 4 for the hexagonal and 8|4 configurations at different thicknesses. First, the dimensional reduction greatly improves the light absorption, for instance, the absorption intensities are at least three times stronger in the monolayer 8|4 than in the bulk 8|4 configuration. Second, the two-layer hexagonal vdW configuration possesses the absorption intensities comparable to or even slightly weaker than the monolayer hexagonal configuration. The band edge absorptions match the band gaps of 3.39 and 3.21 eV at the Γ point for the mono- and two-layer configura-

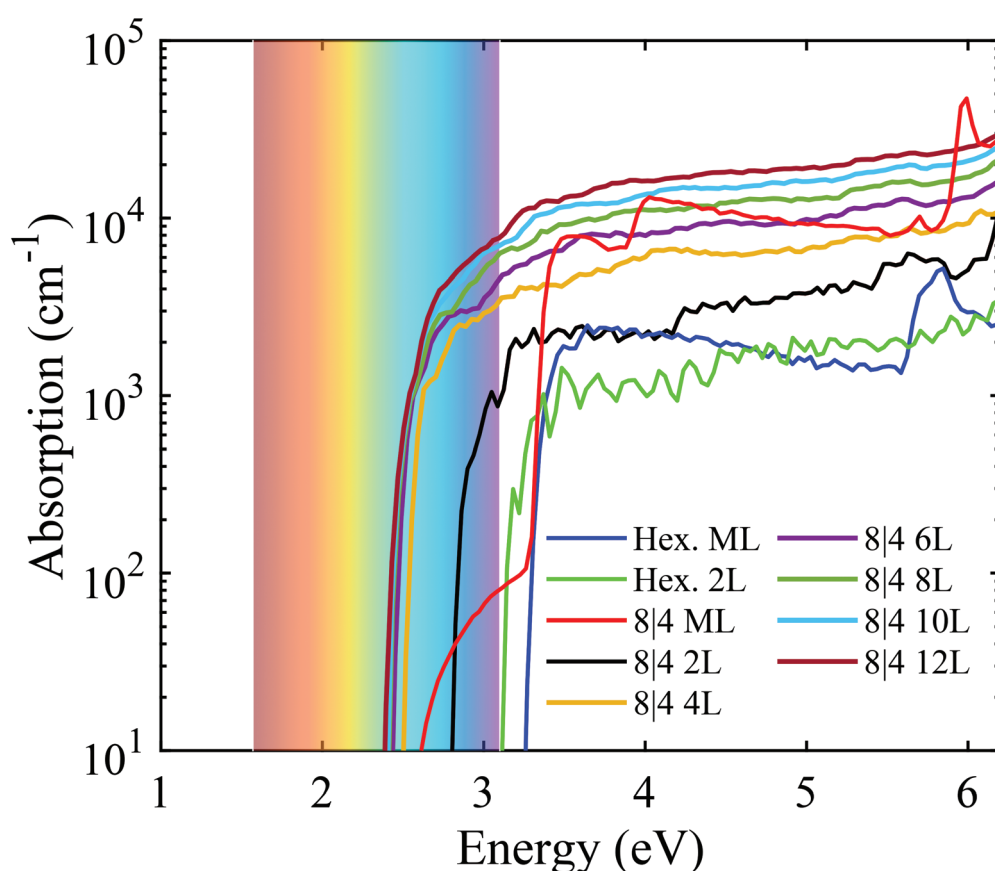


Fig. 4 Optical absorption coefficients in the hexagonal and 8|4 configurations at different thicknesses at the HSE06 level.

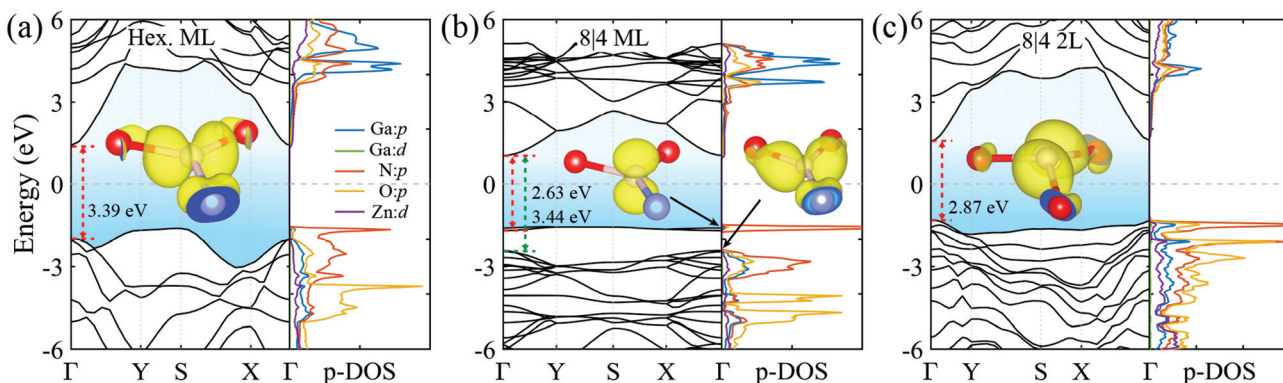


Fig. 5 HSE06 electronic band structures as well as density of states of (a) monolayer hexagonal, (b) monolayer 8|4 and (c) two-layer 8|4 configurations. The spatial valence band edge state distributions are inserted in each panel.

ations, respectively (see Fig. 5(a) and S8(a) in ESI[†]). Therefore, it is difficult to enhance the optoelectronic performance by constructing the vdW configurations from different stacking modes in this system, although such methods have been extensively employed in 2D systems. Third, the 2D 8|4 configurations exhibit stronger absorption intensities than the 2D hexagonal configurations, *e.g.*, at least four times in the monolayer 8|4 than in the monolayer hexagonal structure, attributed to the electron transitions at the Γ point (see Fig. 5(a) and (b)). Similarly, in monolayer GaN and ZnO, the absorption peaks are about five times higher in the 8|4 than in the hexagonal configurations (see Fig. S7 in ESI[†]). This obviously verifies the feasibility to improve the visible-light absorption in the 8|4 configuration through eliminating the IEF. Finally, as the thickness of 8|4 configuration increases, the red shift continuously occurs, while the outstanding absorption intensities remain almost unaffected. The absorption threshold converges to around 2.36 eV at twelve layers, much close to the visible-light absorption. Moreover, the electron–hole interaction is obvious in the multi-layer 8|4 configurations due to the lack of screening in the third dimension, for example, the exciton binding energy of 735 meV in the two-layer 8|4 configuration (see Fig. S2 in ESI[†]).

It is remarkable that the monolayer 8|4 configuration possesses a quite distinct light absorption from other configurations (see Fig. 4). The absorption threshold matches the band gap of 2.63 eV at the Γ point, while the first main absorption peak around 3.44 eV arises from the transitions from the doubly degenerate state of the top third and fourth valence bands to the CBM state at the Γ point, showing a somewhat typical character of indirect band gap structure, as displayed in Fig. 5(b). In other configurations, the main peaks all appear in the vicinity of the absorption thresholds, reflecting the direct-band-gap character. Fig. 5 and S8 and S9 in ESI[†] reveal the anomalous spatial distributions of N-p electrons near the Fermi level. In the monolayer 8|4 configuration, the VBM state at the Γ is fully localized, consistent with the nearly flat top two valence bands, since the N-p_z electrons are isolatedly and symmetrically distributed on both sides of the plane. However,

for the doubly degenerate state, the N-p electrons are obviously distributed on the hybridized orbitals between N and Ga atoms, which greatly promotes the transitions to the CBM state. In other configurations, the hybridized distributions of N-p electrons significantly reduce the effective masses for the VBM state at the Γ (see Table 1), which finally results in the strong absorption intensities.

The HSE06 band structures in the hexagonal configurations and monolayer GaN share the indirect band gaps (see Fig. 5, S7 and S8 in ESI[†]), but the light absorptions exhibit the direct-band-gap characters. The CBMs occur at the Γ point, while the VBMs at other high-symmetry points. Here, we employ the monolayer hexagonal configuration as an example to explore the anomalous behaviors. The VBM is at the S point, the CBM is 2.72 eV higher at the S than at the Γ point. The electron transitions at the S are seriously suppressed, and the main absorption peak occurs at the Γ with the threshold of the band gap of 3.39 eV. Another noteworthy issue is the direct-band-gap structures in the 8|4 configurations at different layers. Previous studies reveal the indirect-band-gap structures in the different-layer 8|4 GaN with the CBMs at the Γ point.^{14,20,21} The total densities of states of the hexagonal and 8|4 configurations,

Table 1 HSE06 electronic band gaps and carrier effective masses in different 2D structures. In the monolayer 8|4 configuration, the electron effective masses are calculated for the doubly degenerate state of the top third and fourth valence bands at the Γ point. The indirect band gaps and the gaps at the Γ point are listed together

Structure	E_g (eV)	Electron (m_0)		Hole (m_0)	
		x	y	x	y
Wurt. bulk	2.34	1.32	0.20	2.13	2.5
8 4 bulk	2.44	0.25	0.83	1.59	5.25
Hex. ML	3.02/3.39	1.79	0.38	4.25	1.15
Hex. 2L	3.16/3.21	0.97	0.30	4.76	1.56
8 4 ML	2.63/3.44	1.24	11.48	11.67	11.24
8 4 2L	2.87	1.17	1.01	1.25	4.05
8 4 4L	2.60	1.24	0.73	1.46	4.61
8 4 6L	2.53	1.30	0.70	1.54	4.83
8 4 8L	2.50	1.36	0.69	1.58	4.93

plotted in Fig. S10 in ESI,[†] reveal that the Ga-d binding energy is much larger than the Zn-d binding energy by at least 7.30 eV, which is insensitive to the configuration and the number of layers. Meanwhile, the VBM at the Γ point are dominated by the N-p states. Therefore, the stronger p-d coupling^{44–47} between Zn and N than between Ga and N atoms pushes the VBM up at the Γ point, and hence leads to the transition from indirect to direct band gap structures.

For the optoelectronic and photovoltaic applications, the heterostructures are routinely adopted to realize the carrier confinements, *e.g.*, GaN/graphene, GaN/SiC and GaN/MoS₂.^{48–50} Here the vdW (vdW-DF2 exchange functional) heterostructures are constructed by integrating the different-layer 8|4 configurations on monolayer MoS₂ due to the nearly negligible lattice mismatch, which is as large as ~30% for graphene. The AA stacking, where the atomically flat saturated surface of MoS₂ matches well with that of the 8|4 configuration, is more energetically favorable than the AB stacking, *e.g.*, by 6.2 meV per atom for the four-layer 8|4 heterostructures (see Fig. 6(a)). After the structural relaxations, the 8|4 structure remains the initial configuration and hence retains good stability. The first-principles molecular dynamic simulations reveal that the heterostructures is thermally stable at room temperature without structural destructions, as displayed in Fig. 6(b).

To explore the light absorptions in the MoS₂-based heterostructures, we first identify how the IEF evolve with the

number of 8|4 layers, according to the significant effects on the band edge states, as shown in Fig. 6(c)–(e). Compared to the freestanding 8|4 configurations, the IEF is greatly reduced by the heterointerfacial coupling in the 8|4 structures of the heterostructures. For instance, the IEF of 0.17 eV m^{−1} in the four-layer 8|4 structure is one fifth of that in the freestanding configuration. Furthermore, the IEF drops more quickly with the number of 8|4 layers in the heterostructures and nearly reaches zero above the six layers. This implies the remarkably better optoelectronic performances in the heterostructures than in the freestanding 8|4 configurations. In addition, the similar results are obtained in the heterostructures composed of the different-layer wurtzite configurations and monolayer MoS₂ (see Fig. S11 in ESI[†]).

Fig. 7(a) shows that the heterostructures share the quite distinct light absorptions from the freestanding 8|4 configurations. First, the visible-light absorptions are greatly enhanced by the abrupt red shifts and the absorption threshold converges to around 1.0 eV above 10 layers in the heterostructure. Second, there are three typical peaks of light absorptions in the heterostructures, while only one main peak in the freestanding 8|4 configurations. The absorption intensities are strengthened at least 4.5 times in the heterostructure, and are comparable to those of other light-absorber materials, *e.g.*, CIGS and hybrid halide perovskites.^{51,52}

To further reveal the light-absorption spectra, we take the four-layer 8|4 heterostructure as an example by calculating the

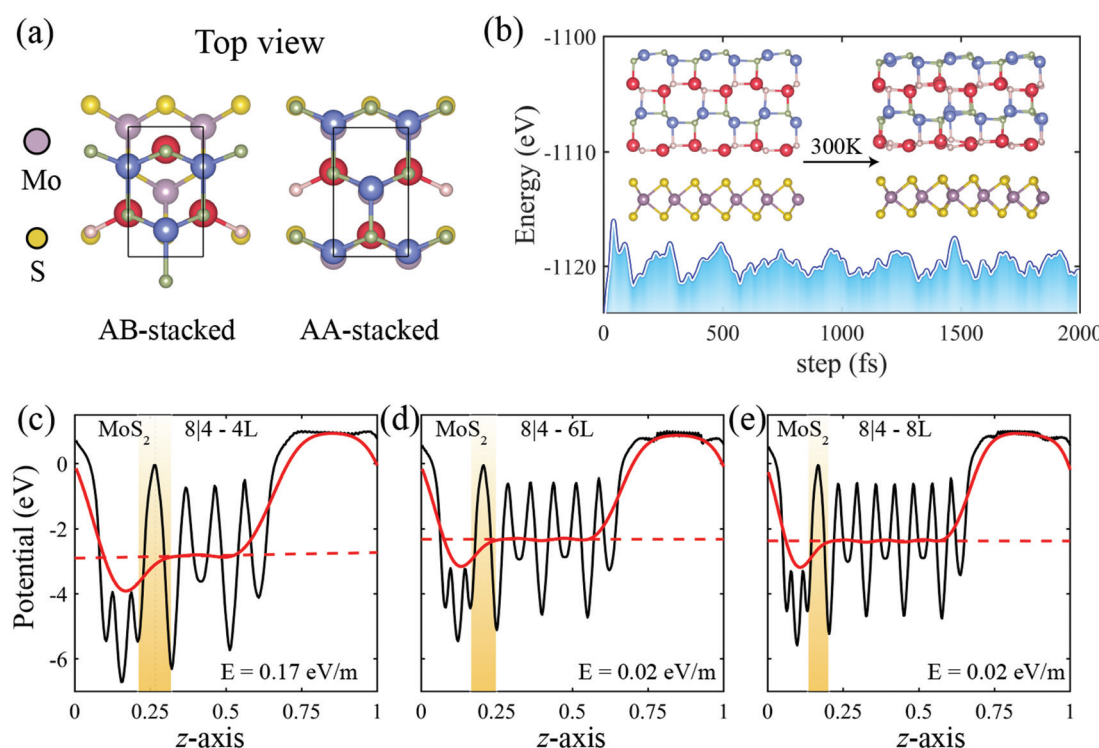


Fig. 6 (a) Top views of AB and AA stacking modes of the MoS₂-based heterostructures along the c axis. (b) The fluctuations of potential energy of the AA-stacking MoS₂-based heterostructure with the four-layer 8|4 configuration at 300 K, together with the snapshots at the start and end of the simulation as insets. (c)–(e) Internal electrostatic potentials for the MoS₂-based heterostructures with the different-layer 8|4 configurations.

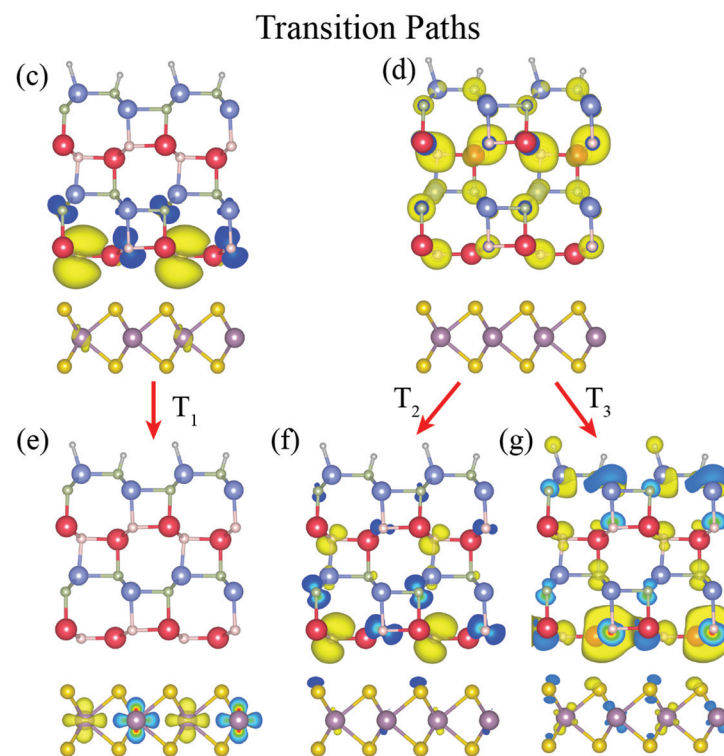
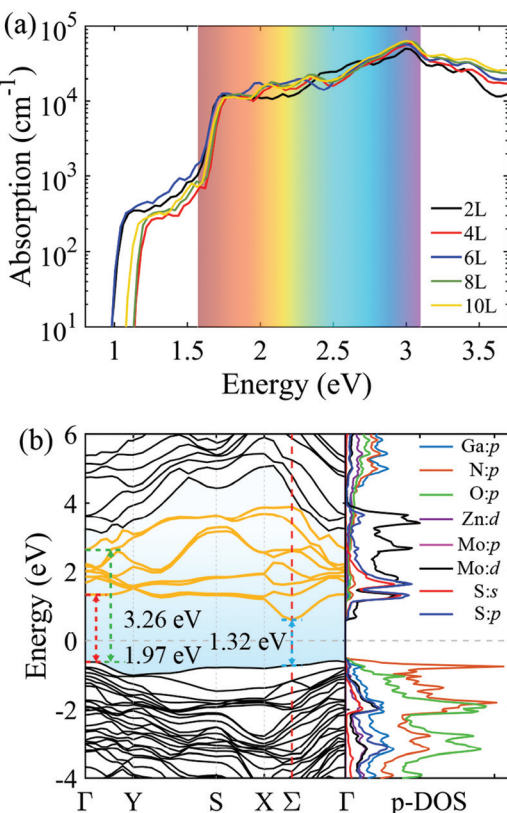


Fig. 7 (a) Optical absorption coefficients in the MoS₂-based heterostructures with the different-layer 8|4 configurations at the HSE06 level. (b) HSE06 electronic band structure and density of states in the MoS₂-based heterostructure with the four-layer 8|4 configuration, together with the spatial band edge state distributions for the valence and conduction bands near the Fermi level at the Γ and Σ points, as shown in panels (c)–(g). The T_1 , T_2 and T_3 symbols indicate the electron-transitions for the main light absorption peaks.

band structure and density of states using the HSE06 functional, as plotted in Fig. 7(b). To remove the effects of the dangling bonds, the top surface is passivated by hydrogen atoms. The indirect band gap appears with the VBM at the Γ point and the CBM at the Σ (0.33,0,0,0) between the X and Γ points. It is interesting that the band gaps are 1.32 and 1.97 eV at the Σ and Γ , respectively, which are much smaller than those of MoS₂ (2.14 eV) and the 8|4 configuration (2.60 eV). This is because that the bottom conduction bands mainly arise from MoS₂ and the top valence bands from the 8|4 configuration, similar to GaN/MoS₂ heterostructure.⁵³ More specifically, the CBM states originate from the Mo d orbitals, and the VBM states are mainly from the N p orbitals, as illustrated by the spatial band edge state distributions at the Σ point (see Fig. 7(c) and (e)). The vdW heterointerface spatially separates the photogenerated electrons and holes, hence, it is difficult for the top valence electrons to the bottom conduction bands by overcoming the vacuum barrier. In addition, Fig. 7(c) reveal that the VBM state near the Σ point displays a somewhat localized character, consistent with the relatively flat top valence band. Therefore, although the p-d electron transitions between N and Mo atoms lead to the abrupt red shift, the absorption intensities are very weak near the absorption threshold.

Fig. 7(b) and S12 in ESI† further reveal that the second and third main absorption peaks arise from the transitions at the Γ point from the VBM state to the CBM state and to the eighth bottom conduction band, respectively. The VBM state at the Γ is dominated by the N p_x electrons, which are mainly distributed between Ga and N atoms, and the strong orbital hybridizations, clearly shown in Fig. 7(d), lead to much dispersive bands. Although the Mo d and S s, p orbitals contribute much to the bottom conduction bands, the CBM state at the Γ point originates from the N p_x, p_y and p_z hybrid orbitals, especially, near the heterointerface, as illustrated in Fig. 7(f). The internal p-p transitions of N atoms are responsible for the strong absorption intensities around 1.97 eV. The eighth bottom conduction band at the Γ point is mainly from the Ga p and N p states, whose densities markedly accumulate near the heterointerface (see Fig. 7(g)), thereby, the light absorption is greatly improved. In addition, the intra-site orbital hybridization pushes the energy up, and hence leads to the strongest light absorption intensities around 3.0 eV. Therefore, although the predominant light absorption is from the internal transitions in the 8|4 configuration, not from the reported transitions between MoS₂ and the 8|4 configurations, the heterointerfacial coupling is a necessary condition to improve the visible-light absorption through accumulating the band edge states.

4. Conclusions

In summary, we have systematically explored the stable bulk and 2D configurations in GaN–ZnO alloys using first-principles structural searches. By reducing the thickness, the wurtzite configuration spontaneously transforms into the 8|4 configuration with the nearly zero IEF, thus the visible-light absorption is greatly improved by eliminating the quantum confined Stark effects. In the novel haeckelite (8|4) configuration, the nearly zero IEF prefers the structural stability, but the structural distortion, a by-product to form the squares, accumulates with the number of layers. In the conventional wurtzite configuration, the tetrahedral coordinations are energetically favorable, but the strong IEF coexists along the *c* axis. The successive structural transitions from the monolayer planar hexagonal to the few-layer 8|4 and to the conventional wurtzite configurations are driven by the comprehensive effects of the IEF and the structural distortions, which are eventually adjusted by the thickness. It is difficult to improve the visible-light absorption by stacking the monolayer planar hexagonal configurations in different modes to construct the vdW structures in this system. Furthermore, in the MoS₂-based heterostructures with the few-layer 8|4 configurations, accompanied with the abrupt red shifts, the visible-light absorptions are remarkably improved, compared to the freestanding 8|4 configurations. The enhanced light absorptions arise not from the reported p–d transitions between N and Mo atoms, but from the internal transitions in the 8|4 configurations, however, the heterointerfacial coupling is a necessary condition to widen optoelectronic applications through accumulating the band edge states. Our results demonstrate that 2D GaN–ZnO alloys exhibit more desirable properties than the binary counterparts and hence show more potentials in designing novel optoelectronic devices.

Conflicts of interest

There are no conflicts to declare.

Acknowledgements

We thank Dr Hongliang Shi at Beihang University for the helpful discussions about the exciton effects. The work is sponsored by the National Natural Science Foundation of China (No. 11774416), the Fundamental Research Funds for the Central Universities (No.2017XKZD08 and 2015XKMS081), the Postgraduate Research & Practice Innovation Program of Jiangsu Province (No. KYCX20_2039) and the Assistance Program for Future Outstanding Talents of China University of Mining and Technology (No. 2020WLJCRCZL063). We are also grateful to the Advanced Analysis and Computation Center of CUMT for the award of CPU hour to accomplish this work.

References

- 1 A. Khan, K. Balakrishnan and T. Katona, *Nat. Photonics*, 2008, **2**, 77.
- 2 Y. Duan, L. Qin, L. Shi, G. Tang and H. Shi, *Appl. Phys. Lett.*, 2012, **100**, 022104.
- 3 Y. Duan, L. Qin, G. Tang and L. Shi, *Eur. Phys. J. B*, 2008, **66**, 201.
- 4 H. Morkoç and S. N. Mohammad, *Science*, 1995, **267**, 51–55.
- 5 P. Walterteit, O. Brandt, A. Trampert, H. T. Grahn, J. Menniger, M. Ramsteiner, M. Reiche and K. H. Ploog, *Nature*, 2000, **406**, 865.
- 6 K. F. Mak, C. Lee, J. Hone, J. Shan and T. F. Heinz, *Phys. Rev. Lett.*, 2010, **105**, 136805.
- 7 A. Splendiani, L. Sun, Y. Zhang, T. Li, J. Kim, C.-Y. Chim, G. Galli and F. Wang, *Nano Lett.*, 2010, **10**, 1271.
- 8 C. L. Freeman, F. Claeysens, N. L. Allan and J. H. Harding, *Phys. Rev. Lett.*, 2006, **96**, 066102.
- 9 H. Şahin, S. Cahangirov, M. Topsakal, E. Bekaroglu, E. Akturk, R. T. Senger and S. Ciraci, *Phys. Rev. B: Condens. Matter Mater. Phys.*, 2009, **80**, 155453.
- 10 D. Xu, H. He, R. Pandey and S. P. Karna, *J. Phys.: Condens. Matter*, 2013, **25**, 345302.
- 11 D. Wu, M. G. Lagally and F. Liu, *Phys. Rev. Lett.*, 2011, **107**, 236101.
- 12 A. Ramasubramaniam, *Phys. Rev. B: Condens. Matter Mater. Phys.*, 2012, **86**, 115409.
- 13 G. Kim, K. Y. Ma, M. Park, M. Kim, J. Jeon, J. Song, J. E. Barrios-Vargas, Y. Sato, Y.-C. Lin, K. Suenaga, S. Roche, S. Yoo, B.-H. Sohn, S. Jeon and H. S. Shin, *Nat. Commun.*, 2020, **11**, 5359.
- 14 A. V. Kolobov, P. Fons, J. Tominaga, B. Hyot and B. André, *Nano Lett.*, 2016, **16**, 4849.
- 15 P. Tsipas, S. Kassavetis, D. Tsoutsou, E. Xenogianopoulos, E. Golias, S. A. Giamini, C. Grazianetti, D. Chiappe, A. Molle, M. Fanciulli and A. Dimoulas, *Appl. Phys. Lett.*, 2013, **103**, 251605.
- 16 W. Wang, Y. Zheng, X. Li, Y. Li, H. Zhao, L. Huang, Z. Yang, X. Zhang and G. Li, *Adv. Mater.*, 2019, **31**, 1803448.
- 17 Z. Y. Al Balushi, K. Wang, R. K. Ghosh, R. A. Vilá, S. M. Eichfeld, J. D. Caldwell, X. Qin, Y.-C. Lin, P. A. DeSario, G. Stone, S. Subramanian, D. F. Paul, R. M. Wallace, S. Datta, J. Redwing and J. A. Robinson, *Nat. Mater.*, 2016, **15**, 1166.
- 18 H. Baek, C.-H. Lee, K. Chung and G.-C. Yi, *Nano Lett.*, 2013, **13**, 2782.
- 19 C. Tusche, H. L. Meyerheim and J. Kirschner, *Phys. Rev. Lett.*, 2007, **99**, 026102.
- 20 Y. Jia, Z. Shi, W. Hou, H. Zang, K. Jiang, Y. Chen, S. Zhang, Z. Qi, T. Wu, X. Sun and D. Li, *npj 2D Mater. Appl.*, 2020, **4**, 31.
- 21 A. V. Kolobov, P. Fons, Y. Saito, J. Tominaga, B. Hyot and B. André, *Phys. Rev. Mater.*, 2017, **1**, 024003.
- 22 E. Gürbüz, S. Cahangirov, E. Durgun and S. Ciraci, *Phys. Rev. B*, 2017, **96**, 205427.

- 23 K. Maeda, K. Teramura, D. Lu, T. Takata, N. Saito, Y. Inoue and K. Domen, *Nature*, 2006, **440**, 295.
- 24 K. Maeda, T. Takata, M. Hara, N. Saito, Y. Inoue, H. Kobayashi and K. Domen, *J. Am. Chem. Soc.*, 2005, **127**, 8286.
- 25 A. R. Oganov, Y. Ma, A. O. Lyakhov, M. Valle and C. Gatti, *Rev. Mineral. Geochem.*, 2010, **71**, 271–298.
- 26 A. O. Lyakhov, A. R. Oganov, H. T. Stokes and Z. Qiang, *Comput. Phys. Commun.*, 2013, **184**, 1172.
- 27 J. P. Perdew, K. Burke and M. Ernzerhof, *Phys. Rev. Lett.*, 1996, **77**, 3865–3868.
- 28 W. Kohn and L. J. Sham, *Phys. Rev.*, 1965, **140**, A1133–A1138.
- 29 G. Kresse and J. Hafner, *Phys. Rev. B: Condens. Matter Mater. Phys.*, 1993, **47**, 558–561.
- 30 G. Kresse and J. Furthmüller, *Phys. Rev. B: Condens. Matter Mater. Phys.*, 1996, **54**, 11169–11186.
- 31 J. Klimeš, D. R. Bowler and A. Michaelides, *J. Phys.: Condens. Matter*, 2009, **22**, 022201.
- 32 L. Chaput, A. Togo, I. Tanaka and G. Hug, *Phys. Rev. B: Condens. Matter Mater. Phys.*, 2011, **84**, 094302.
- 33 W. Jia, J. Fu, Z. Cao, L. Wang, X. Chi, W. Gao and L.-W. Wang, *J. Comput. Phys.*, 2013, **251**, 102–115.
- 34 W. Jia, Z. Cao, L. Wang, J. Fu, X. Chi, W. Gao and L.-W. Wang, *Comput. Phys. Commun.*, 2013, **184**, 9–18.
- 35 J. Heyd, G. E. Scuseria and M. Ernzerhof, *J. Chem. Phys.*, 2003, **118**, 8207–8215.
- 36 T. Sander, E. Maggio and G. Kresse, *Phys. Rev. B: Condens. Matter Mater. Phys.*, 2015, **92**, 045209.
- 37 D. F. Blossey, *Phys. Rev. B: Solid State*, 1970, **2**, 3976–3990.
- 38 J. D. Dow and D. Redfield, *Phys. Rev. B: Solid State*, 1970, **1**, 3358–3371.
- 39 J. Zhu, S. Ban and S. Ha, *Superlattices Microstruct.*, 2013, **56**, 92–98.
- 40 R. J. Elliott, *Phys. Rev.*, 1957, **108**, 1384–1389.
- 41 A. T. Winzer, G. Gobsch, R. Goldhahn, D. Fuhrmann, A. Hangleiter, A. Dadgar and A. Krost, *Phys. Rev. B: Condens. Matter Mater. Phys.*, 2006, **74**, 125207.
- 42 See ESI at http://*** for more details on the enthalpy differences, structural parameters, phonon spectrums, electronic band structures, convex hulls, band gaps, density of states, crystal structures, and elastic parameters.†
- 43 Y. Darici, T. Wolfram, H. R. Chandrasekhar and D. Cowan, *Phys. Rev. B: Condens. Matter Mater. Phys.*, 1988, **38**, 9686–9693.
- 44 J. E. Jaffe and A. Zunger, *Phys. Rev. B: Condens. Matter Mater. Phys.*, 1983, **28**, 5822–5847.
- 45 J. E. Jaffe and A. Zunger, *Phys. Rev. B: Condens. Matter Mater. Phys.*, 1984, **29**, 1882–1906.
- 46 W. Liu, H. Liang, Y. Duan and Z. Wu, *Phys. Rev. Mater.*, 2019, **3**, 125405.
- 47 X. Chen, W. Liu and Y. Duan, *J. Phys.: Condens. Matter*, 2021, **33**, 075401.
- 48 Y. Gohda and S. Tsuneyuki, *Appl. Phys. Lett.*, 2012, **100**, 053111.
- 49 D. Ruzmetov, K. Zhang, G. Stan, B. Kalanyan, G. R. Bhimanapati, S. M. Eichfeld, R. A. Burke, P. B. Shah, T. P. O'Regan, F. J. Crowne, A. G. Birdwell, J. A. Robinson, A. V. Davydov and T. G. Ivanov, *ACS Nano*, 2016, **10**, 3580.
- 50 A. Yamada, K. Ho, T. Maruyama and K. Akimoto, *Appl. Phys. A: Mater. Sci. Process.*, 1999, **69**, 89.
- 51 M. R. Kim and D. Ma, *J. Phys. Chem. Lett.*, 2015, **6**, 85.
- 52 M. A. Green and S. P. Bremner, *Nat. Mater.*, 2017, **16**, 23.
- 53 J. Wang, H. Shu, P. Liang, N. Wang, D. Cao and X. Chen, *J. Phys. Chem. C*, 2019, **123**, 3861.